Salinity control of thermal evolution of late summer melt ponds on Arctic sea ice

Joo-Hong Kim[1], Woosok Moon[2,3], Andrew J. Wells[4], Jeremy P. Wilkinson[5], Tom Langton[4], Byongjun Hwang[6,7], Mats A. Granskog[8] and David Rees Jones[9]

[1]Korea Polar Research Institute, Incheon, South Korea
[2]Nordic Institute for Theoretical Physics, Stockholm, Sweden
[3]Department of Mathematics, Stockholm University, Stockholm, Sweden
[4]Atmospheric, Oceanic and Planetary Physics, University of Oxford, Oxford, UK
[5]British Antarctic Survey, Cambridge, UK.
[6]Scottish Association for Marine Science, Oban, UK
[7]University of Huddersfield, Huddersfield, UK
[8]Norwegian Polar Institute, Fram Centre, Tromsø, Norway
[9]Dept. of Earth Sciences, University of Oxford, Oxford, UK

Corresponding author: Joo-Hong Kim (joo-hong.kim@kopri.re.kr)

Key Points:

- Salinity variations within melt ponds on sea-ice result in different thermal evolution and heat transfer to the ice below
- Turbulent thermal convection drives heat transfer in freshwater ponds, while conduction is more significant in salt-stratified ponds
- Predicted differences in heat flux are of the order of several W m^{-2}, which is of potential climatological significance for sea-ice evolution

Abstract The thermal evolution of melt ponds on Arctic sea-ice was investigated through a combination of autonomous observations, and two-dimensional high-resolution fluid dynamics simulations. We observed one relatively fresh pond and one saline pond on the same ice floe, with similar depth. The comparison of observations and simulations indicates that thermal convection dominates in relatively fresh ponds, but conductive heat transfer dominates in salt-stratified ponds. Using a parameterized surface energy balance, we estimate that the heat flux to the ice is larger under the saline pond than the freshwater pond when averaged over the observational period. The deviation is sensitive to assumed wind, varying between 3–14 W m^{-2} for winds from 0–5 m s^{-1}. If this effect persists as conditions evolve through the melt season, our results suggest that this imbalance potentially has a climatologically-significant impact on sea-ice evolution.

1 Introduction

One of the most dramatic winter-to-summer transformations of Arctic sea-ice is the formation and progression of melt ponds on the ice surface. Melt ponds, which can cover a significant fraction of the ice surface in summer (Fetterer & Untersteiner, 1998; Perovich et al., 2002b; Polashenski et al., 2012; Divine et al., 2015), lower the surface albedo and increase the absorption of shortwave radiation and transmission through ice into the underlying ocean (e.g., Curry et al., 1995; Hanesiak et al., 2001; Perovich et al., 2002a; Perovich et al., 2007; Frey et al., 2011; Perovich & Polashenski, 2012; Nicolaus et al., 2012, Hudson et al., 2013). Heat fluxes in ponds and their role in the ice-albedo feedback form a major component of the sea-ice energy balance and considerably intensify summer melt (Stroeve et al., 2014).

A simple treatment of ponds in sea-ice models parameterizes the albedo as a function of the mean depth, available water, and areal fraction of ponds (Ebert & Curry, 1993) assuming uniform pond temperature. Thus, melt ponds only affect the surface albedo in the energy flux balance. Taylor and Feltham (2004; hereafter TF04) included a radiative transfer model for shortwave radiance in the pond–ice system, and potentially turbulent heat fluxes in the pond interior (internal heating by the absorption of shortwave radiation can lead to convective instability inside a freshwater pond). In TF04, weak buoyancy forcing results in sensible heat fluxes through the pond from conduction, while strong buoyancy forcing is described through a scaling law for turbulent convective boundary layers at the top and bottom of the pond. These parameterizations may provide a better treatment of the surface energy flux balance in climate models. However, their treatment of the thermal characteristics of the pond interior have not been validated against *in situ* observations. Particularly, melt ponds occur in a range of salinities, 0–29 ppt (Perovich et al., 2009; Lee et al., 2011), which may affect the stratification of the ponds and the consequent surface energy balance.

This study investigated whether the salinity of ponds modifies their thermal evolution, with subsequent impacts on net heat fluxes. We describe *in situ* measurements (section 2) of shortwave radiation and vertical temperature profiles within two adjacent ponds of differing salinity, over 3 weeks in August 2015. The evolving temperature profiles are compared to numerical simulations of fluid flow and heat transfer in a model pond (section 3). This comparison is consistent with a radiative-convective balance in a relatively fresh pond, and a radiative-conductive balance in a

saline stratified pond. We estimate that the changing heat fluxes may provide a climatologically significant modification of the sea-ice energy budget (section 4).

2 Observations

2.1 Deployment

On August 12, 2015, an ice station was established (80.4 °N, 172.4 °E) north of the East Siberian Sea (Figure 1a). The chosen floe was located well away from the ice edge, contained numerous melt ponds, and comprised of both first-year ice (FYI) and multi-year ice (MYI); (Figure 1b). An ice mass balance buoy with radiometers (IMB-R) was installed in one relatively fresh pond of 2.3 g kg^{-1} bottom salinity and 1.1 g kg^{-1} near-surface salinity (measured by salinometer YSI Model 30, Accuracy of ±2 %). We refer to this as a freshwater pond hereafter. Another IMB-R was deployed in a separate more saline pond of 20 g kg^{-1} bottom salinity and 14 g kg^{-1} near-surface salinity (Figures 1c–d). This IMB-R updates the system described by Jackson et al. (2013) with 0.0078 K resolution thermistors (ADT7320, Analog Devices). The IMB-Rs were equipped with shortwave radiometers: two in air (SP-230, Apogee) and one below the ice (SP-110). Among the hourly measurements, incident downward shortwave fluxes are presented here. In addition, webcam photographs taken every 6 hours document the evolution of the pond and weather. Thermistor chains were suspended vertically from a wire extended across the pond (Figure 1d), down through a 5-cm wide borehole drilled through the ice beneath the pond. The ponds showed no detectable drainage through the hole, indicating that they were at sea level. Hourly vertical temperature profiles were measured at 2 cm intervals through the air above, the pond, the underlying borehole, and into the ocean below. Our analysis focuses on the water temperature in the pond interior.

Upon deployment (August 12), the freshwater pond was 23 cm deep at the deployment point, with light-blue color and a thin layer of ice on the surface (Figures 1b–c). The surface ice cover around the IMB-R was broken and removed during deployment. The saline pond was 22 cm deep at the deployment point, with dark-blue color and no surface ice (Figures 1b–c). The ice thickness below the freshwater pond was 219 cm, and 100 cm under the saline pond. This suggests that the freshwater pond was formed on thicker MYI, with the saline pond on thinner FYI. The difference in ice thickness affected the pond bottom albedo; the albedo of the saline pond (on thinner ice) was much lower than that of the freshwater pond. Temperature profiles were measured until a polar

bear damaged the IMB-R in the freshwater pond. We therefore focus on the common observation period from August 13 to 29.

2.2 Meteorological conditions

The air temperature above the ponds was calculated by averaging the top 10 thermistors in air (Figure 2a). The two IMBs recorded almost identical variations in air temperature, which is to be expected given their short separation (~70 m; Figure 1b).

We identify three main periods P1–P3 reflecting different meteorological conditions based on the air temperatures, incident shortwave radiative fluxes (Figures 2a–b), and webcam photographs (supporting Figure S1, Movie S1). These are:

- P1 (August 14–19): Air temperature hovered around freezing during an overcast period. There was a weak diurnal cycle in pond temperature, which was slightly enhanced on August 16–17 due to nighttime reduction of cloud cover.

- P2 (August 19–25): Clear skies prevailed. This resulted in a significantly enhanced diurnal signal and lower atmospheric temperatures, consistent with the loss of cloud cover and strong nighttime infrared cooling. The photographs (Figure S1, Movie S1) show signs of nighttime snowfall on August 22.

- P3 (August 25–29): The clouds returned with several snowfall events between 27–29 August and temperatures below freezing (Figure 2a).

The incident shortwave fluxes show similar temporal variation for both ponds during cloudy conditions (P1, P3 in Figure 2b), but diverge during P2 when the ponds receive high insolation. The photographs suggest that the radiometer in the saline pond tilted over several days (Figure S1, Movie S1), which likely explains the bias in fluxes on days with clear sky and strong incident solar radiance. Thus, the upright sensor at the freshwater pond provides the better measure of varying incident shortwave radiation.

2.3 Pond water temperature

The changing meteorological forcing drives thermal variability, with significant differences between the ponds (Figure 2c–f vs. 2g–j). The water temperature at the base of both ponds approaches their salinity determined freezing point (Perovich et al., 2009); about 0 °C for the freshwater pond, and around −1.1 °C for the saline pond of 20 g kg^{-1} salinity. The mean temperature of the saline pond was typically 0.5 °C to 1.2 °C colder than the freshwater pond, likely partly due to the difference in freezing point at the lower boundary. In addition, the higher shortwave reflection at the bottom of the freshwater pond (Figure 1b) potentially enhances the radiative heating of that pond compared to the darker saline pond. The saline pond was likely interconnected (through a network of ponds) to the ocean (Figure 1b), which may allow lateral exchange with colder seawater. As the ice thins the freeboard lowers, allowing for flooding of

shallow interconnected ponds (Polashenski et al., 2012). FYI, being thinner, will be more susceptible to this process.

The temperature profiles of both ponds exhibit a significant diurnal response to daytime shortwave heating and nighttime surface cooling (see Figures 2c, 2g and anomaly plots in supporting Figure S2), but show notably different thermal structures, indicating differing efficiencies of heat transfer.

During the warm and cloudy period P1, the saline pond shows a strong thermal gradient (Figure 2d) and evidence of a phase lag in the propagation of heat downward through the pond (August 15–17 in Figure 2c). The salinity measurements suggest strong stratification within the saline pond, like previous observations from other saline ponds (Perovich et al., 2009), indicating relatively inefficient diffusive heat transfer. By contrast, the freshwater pond displays a vertical temperature curve with minima at top and bottom (a reversed C-shape; Figure 2h) and a more synchronous temporal response with depth, indicating efficient thermal transfer (Figure 2g). We hypothesize that the different thermal structures result from a radiative-conductive balance in a salt-stratified pond, and more efficient turbulent convective mixing in the freshwater pond, as explored in section 3.

The first half of P2 (up to August 22) was cold with clear skies, and a significant mid-depth temperature maximum develops in both ponds (Figures 2e, 2i). This is consistent with heating by radiative absorption, accompanied by strong net surface heat losses due to reduced downwelling longwave in the absence of clouds. In the second half of P2, the surface of both ponds froze, and accumulated snow (Figure S1). The diurnal variability diminished, despite large daytime incoming shortwave fluxes comparable to the first half of P2. The ice and snow layer on the ponds significantly reduces transmission of shortwave radiation into the pond, muting the diurnal cycle of heating and cooling (Figures 2c, 2i and Figures S2c–d).

During the cold and cloudy period P3, there is a weak thermal response (Figures 2f, 2j), with air temperatures below freezing maintaining an ice lid. The photographs (Figure S1) suggest an optically reflective snow cover accumulated on the freshwater pond. Snow accumulation is more limited on the saline pond (possibly due to brine on the ice surface dissolving newly fallen snow).

3 Idealized model of heat transfer in a melt pond

3.1 Model configuration

To build insight into the physical mechanisms controlling the observed pond temperatures, we calculate sensible and radiative heat transfer through the interior of modeled ponds of differing salinity. Model details are described in the supporting §S2, with key features summarized here. We focus on the period before surface freezing, and model temperature T in a shallow pond of uniform depth H and wide extent in a horizontally-periodic domain. The absorption of shortwave radiation leads to internal heating $Q(z)$ that depends on height z above the pond base (Figure 3a), approximated using the two-stream radiation model described in Skyllingstad and Paulson (2007; SP07 hereafter). The pond base is at the salinity-dependent melting temperature T_m. The energy flux conducted to the upper pond surface balances the sum of longwave, sensible and latent heat

fluxes, which crucially depend on the surface temperature $\boldsymbol{T_s}$. Following Hitchen and Wells (2016), we linearize this surface boundary condition

$$\boldsymbol{k\frac{\partial T}{\partial z} = -F_0 - \gamma(T_s - T_m)} \qquad \text{(at} \quad \boldsymbol{z = H}\text{)}, \qquad (\mathbf{1})$$

where k is the thermal conductivity of water, F_0 is the net flux at temperature $T = T_m$ (positive upward) and the constant $\boldsymbol{\gamma}$ characterizes the sensitivity of net outgoing fluxes to $\boldsymbol{T_s}$. To characterize the relative effects of the surface heat loss versus interior heating we define the ratio $\boldsymbol{f = F_0/Q_0H}$, where $\boldsymbol{Q_0H}$ is the flux due to depth-integrated radiative absorption. The value of f varies diurnally and with the meteorological conditions. Based on our observed fluxes and those from the SHEBA campaign (Stramler, 2006) we often expect f to be smaller in warm and cloudy conditions (where significant downwelling longwave fluxes lead to a low net surface flux), than under clear skies (where the surface energy budget is dominated by large longwave emissions). For example, Figures 3.34–3.35, and 3.32 in Stramler (2006) illustrate small net longwave fluxes approaching zero (of order ±20 W m^{-2}) during cloudy summer days, versus larger net longwave losses of order 20–80 W m^{-2} under clear skies. Using the SP07 radiative model, the shortwave fluxes in Figure 2b and from SHEBA yield diurnal maxima of order $\boldsymbol{Q_0H \sim 100 - 300}$ W m$^{\mathbf{-2}}$ with synoptic variability mostly within 50 % of the diurnal peak value. Seasonally varying pond depth H also impacts f.

When the entire pond is stably stratified, sensible heat transfer occurs via conduction. We solve the heat equation with internal source $Q(z)$ (see supporting §S2a). In ponds with a convectively unstable density stratification, we solve for heat transfer by turbulent convection using direct numerical simulations of the two-dimensional Boussinesq Navier-Stokes equations, and heat transfer by advection, diffusion, and imposed internal heating (see supporting §S2b). We compare a freshwater pond and saline pond of uniform 20 g kg^{-1} salinity. The density $\boldsymbol{\rho(T)}$ is calculated using a nonlinear equation of state (McDougall & Barker, 2011); see Figures 3b–c. A stress-free upper surface corresponds to negligible wind, and we impose no-slip at the pond-ice boundary. The simulations use the *Dedalus* spectral code (Burns et al., 2016). Our configuration shares several similarities with the pioneering work of SP07, with the key differences being the present use of a direct numerical simulation without a turbulence closure, a horizontally periodic domain, and the temperature-dependent surface flux balance (1). SP07 also considered strong winds, which act to nearly homogenize the pond close to the melting temperature. Our observations show significant internal variation of pond temperature and no evidence of wind-driven waves/ripples in the webcam images (Figure S1). Wind speed measurements on *Araon* at 23 m above sea level and distance 0.1-740 km while leaving the ice camp ranged between 2 and 8 m s^{-1} for 5 days during P1. Comparison to climatology from the ERA-Interim reanalysis shows that this range of wind speeds are frequently observed during the summer melt-pond season (June–August), although August 2015 had slightly lower winds (Figure S3). We therefore focus on conditions with low winds, neglecting wind stress.

The available observational data do not fully constrain the model forcing, preventing an exact comparison. Hence we instead explore the sensitivity of pond temperature to absorption of incoming shortwave fluxes $\boldsymbol{Q_0H}$ and outgoing baseline surface fluxes F_0 in illustrative case studies of different dynamical regimes. While diurnal variations are relevant in general, we build initial insight by focusing on statistically steady states. As illustrated in supporting §S2, convective

ponds adjust on a convective timescale of order 100 s that is fast compared to a diurnal period, and so we expect to observe a quasi-steady state for given forcing. For stably stratified ponds the higher-order corrections for diurnally-forced diffusion superimpose vertical propagation of the heating pulse onto the quasi-steady state (Figure S5).

3.2 Model results

For ponds without salt stratification, the internal heating drives convection within the pond, with contrasts between freshwater and saline ponds (Figures 3d–f) due to the nonlinear equation of state. Below 4°C, the density of freshwater increases with temperature, and so colder buoyant plumes detach from the lower boundary layer and rise through the warmer pond interior (Figure 3d, Movie S2). Due to surface cooling, the upper boundary layer below the surface is convectively stable (with colder lighter fluid above the warmer denser interior) and intermittently eroded by rising plumes. The turbulent heat transport occurs via a fundamentally asymmetric mode of convection.

Averaged temperature profiles for the freshwater pond (Figure 3e) show that both the interior and free surface temperature increase with absorbed shortwave flux. The simulations of thermal convection qualitatively capture key features of the thermal structure seen in daytime observations (Figures 2h, S2b) with an internal temperature maximum, significant mixing of absorbed heat through the warm pond interior, and colder upper and lower boundary layers. Moving into the cold period (Figure 2i) the simulation still produces an interior maximum although the observed curvature of $T(z)$ is more pronounced. The current simulation of convection is no longer valid when surface temperatures drop below freezing and an ice lid forms. While the present simulations of convection do not incorporate a diurnal cycle, or knowledge of the spectral quality of the shortwave radiation, it is encouraging that they capture the qualitative vertical structure. The observed temperatures are also similar in magnitude to the range of $T(z)$ seen as the absorbed shortwave flux is varied in simulations (e.g., Figure 3e shows ~0.4 °C warming for a freshwater pond with incoming shortwave flux of order 100 W m^{-2}).

Interestingly, the saline pond shows different thermal variation (Figures 3f–g) compared to the freshwater pond. A leading-order difference arises because the lower ice boundary is at the salinity-dependent melting point (−1.1 °C at 20 g kg^{-1} salinity). Internal heating causes temperature variation relative to this baseline. For a pond of uniform 20 g kg^{-1} salinity, the illustrated heating rate produces similar convective dynamics to the freshwater pond. However, for larger heating the temperature range crosses the density maximum in Figure 3c, and generates convection from the top down (Movie S3).

The average temperature profile for convection in a uniform-salinity pond (solid line in Figure 3g) has similar vertical structure to the freshwater pond, and is not qualitatively consistent with the observed strong thermal gradient in the saline pond during the warm cloudy period P1 (Figure 2d). We contrast with ponds with a strong stabilizing salt stratification and sensible heat transfer dominated by conduction (dashed lines in Figure 3g for three values of f). For sufficiently weak net surface fluxes (e.g., $f = 0.25$) the profiles have strong interior thermal gradient with a shallow cool surface boundary layer. This echoes the observed strong temperature gradients seen in the saline pond during the warm cloudy period P1 (Figure 2d), where significant downwelling longwave fluxes likely lead to a small value of f. For larger f, a greater fraction of heat is lost from

the top boundary, and the surface boundary layer has greater depth. This qualitatively resembles the more pronounced curvature of $T(z)$ observed on clear days in P2 (Figure 2e), where the surface energy budget is dominated by large longwave emissions leading to larger f. Hence, while we lack sufficient observational constraints on the fluxes for an exact comparison, our parameter exploration recovers states consistent with convective heat transfer in the freshwater pond, and conduction in a salt-stratified pond.

4 Discussion

Our field measurements show temperature variation in late summer melt ponds in the range $-1.1\ °C < T < 1.5\ °C$, with diurnal and synoptic variability, and significant differences between freshwater and saline ponds. This thermal variation is indicative of subtle but significant changes to pond heat transfer. When averaged over long timescales during periods without continuous surface ice cover, the change in heat storage in the pond is small compared to the incoming and outgoing fluxes. In a statistically steady state, the absorbed shortwave flux $\boldsymbol{Q_0 H}$ must balance the sum of outgoing fluxes $\boldsymbol{F_0 + \gamma(T_s - T_m)}$ from (1), and the flux conducted down into the ice below the pond. Hence, changing pond surface temperature directly correlates with a net change to the heat flux down into the ice that contributes to ice melt. Any persistent model bias in $\boldsymbol{T_s}$ will lead to persistent bias in the predicted fluxes into the ice. Accounting for longwave emissions alone (i.e., negligible wind) the observed variability of $-1.1\ °C < T_s < 0.9\ °C$ (±0.07 °C standard deviation of uncertainty; see supporting §S3) provides a corresponding net flux perturbation of order $\boldsymbol{-5\ W\ m^{-2} \leq \Delta F \leq 4\ W\ m^{-2}}$ (±0.3 W m^{-2} propagated uncertainty) compared to assuming $T_s = 0$ °C. This may be augmented substantially by the impact of sensible heat fluxes on $\boldsymbol{\gamma}$, which could increase the magnitude of $\boldsymbol{\Delta F}$ by a factor of approximately 6 for 10-m wind speed of 5 m s^{-1} (see supporting §S2a).

The flux difference between freshwater and saline ponds is of particular interest. We estimate differences in outgoing fluxes ($\boldsymbol{\Delta F_s}$) over a 7-day period before continuous surface freezing, using (1) and the observed T_s (see supporting §S3). Note that this difference depends on the impact of sensible heat fluxes on $\boldsymbol{\gamma}$, which is underconstrained by the observations. Accounting for longwave emissions alone yields a time-averaged difference $\boldsymbol{\Delta F_s}$ = 2.2±0.3 W m^{-2} for outgoing fluxes with temporal standard deviation 1.0 W m^{-2} and range $-0.3 \leq \boldsymbol{\Delta F_s} \leq 6.5$ W m^{-2}. With 5 m s^{-1} winds, the above estimates increase by a factor of 5.7 (see supporting §S2a) yielding a mean $\boldsymbol{\Delta F_s}$ = 12.5±1.8 W m^{-2}. The lower surface heat loss in the saline pond combines with declining pond heat storage (equivalent to an average flux 1.114±0.005 W m^{-2} difference; see §S3) to yield a significant additional heat flux down into the ice under saline ponds versus freshwater ponds (estimated average difference of 3.3±0.3 W m^{-2} for zero wind, rising to 13.6±1.8 W m^{-2} at 5 m s^{-1} winds). This will drive faster melt under the saline pond. These estimates have similar order of magnitude to an illustrative example from the time-averaged simulation results (Figure 3) with $\boldsymbol{f = 0.5}$ and modest heating $\boldsymbol{Q_0 H}$ = 20 W m^{-2}. With this forcing, the ice under the saline pond receives 2.5 W m^{-2} additional heat flux compared to the ice under the freshwater pond, in otherwise identical conditions with perfectly matching incoming radiative fluxes, atmospheric conditions, pond geometry and basal albedo. These surface temperatures, heat fluxes into the ice, and their difference between freshwater and salt-stratified ponds will vary with the forcing conditions including incoming radiative fluxes and surface fluxes (e.g., see Figure 3e and 3g), as well as with

pond depth and basal albedo. While the above figures need to be weighted against temporal variability and areal coverage of ponds, they are potentially significant in magnitude compared to the net flux imbalance of only 1 W m^{-2} needed to thin the ice cover by approximately 1 meter per decade (Kwok & Untersteiner, 2011). Importantly, while there are larger individual incoming and outgoing flux components in the energy balance, such fluxes are subject to compensation by the longwave feedback (Moon & Wettlaufer, 2011) while the above flux perturbation from internal pond dynamics is a net anomaly after accounting for longwave feedbacks.

Of particular significance is that many melt-pond parameterizations in climate models assume T_s = 0 °C (e.g., schemes based on Ebert & Curry, 1993; Pedersen et al., 2009; Hunke et al., 2015). This leads to a persistent overestimation of heat fluxes into the ice for freshwater ponds with T_s > 0 °C, and either an over or underestimation of such fluxes for saline ponds depending on the internal heating. More sophisticated models use parameterizations of turbulent heat fluxes across upper and lower convective boundary layers (TF04; Flocco et al., 2007). This offers a valuable framework for accounting for turbulent fluxes in ponds, but our simulations reveal that any convection is fundamentally asymmetric with an upper stable layer in relatively fresh ponds. Indeed, the TF04 parameterization of convective heat transfer predicts T_s = 0 °C when f = 0.5, as a result of the assumed symmetry of convective dynamics between the upper and lower boundary layers, while our simulations predict non-zero T_s. Our results illustrate the importance of accurately accounting for pond salinity and internally heated convection in the next generation of melt-pond parameterizations, to reduce the uncertainty associated with sea-ice projections.

Our estimates come with the caveat that they are based on a moderate observational duration in late summer. While similar physical processes operate throughout the pond season, the strength of environmental forcing varies. In particular, the spectral composition of shortwave fluxes impacts depth-dependent heat absorption, pond depth and salinity vary, and changing meteorological conditions impact surface fluxes. It also remains a curiosity that the observed thermal structure could be recreated in the absence of wind-driven mixing, which acts to homogenize pond temperature (SP07). Pond surfaces have short fetch and low elevation, and we speculate that they may experience lower stress than the surrounding ice. Investigating these and other factors presents interesting avenues for future work.

5 Conclusions

We have observed significant thermal variability in melt ponds on Arctic sea-ice in late summer, with a diurnal cycle and variation between days with cloudy or clear skies. Thermal variation is reduced after a surface ice lid forms and is covered by reflective snow. Temperature profiles also differ between relatively fresh and saline ponds on the same ice floe, despite similar depth and insolation, yielding a larger pond-ice heat flux under the saline pond. The comparison to model simulations is consistent with a radiative-convective balance operating in freshwater ponds, and a radiative-conductive balance in ponds with strong salt-stratification.

The resulting variations of pond surface temperature T_s perturb the pond energy budget significantly compared to the flux needed to thin the ice cover by 1 meter per decade. Hence the internal redistribution and emission of heat from a melt pond augments the usual ice-albedo

feedback, and is of potential climatological significance. This feedback from internal heat transfer is not fully accounted for in typical parameterizations of melt pond processes. The melt pond salinity and salt-stratification are key variables influencing the pond energy budget that are important to constrain in future observations and models. This is particularly important as saline ponds preferentially form on first year ice (Lee et al., 2011), and may increase in prominence as the Arctic transitions to a more seasonal ice cover.

Acknowledgments and Data

J.-H.K. was supported by the K-AOOS (KOPRI, PM18040, 20160245) project, funded by the MOF, Korea, and the KPOPS (KOPRI, PE18130) project. A.J.W. and D.R.J. acknowledge support from the John Fell Oxford University Press Research Fund and thank the Isaac Newton Institute for Mathematical Sciences for hospitality (EPSRC Grant EP/K032208/1). A.J.W. acknowledges European Union Award PCIG13-GA-2013-618610 SEA-ICE-CFD. T.L. was supported by the Oxford-Met Office Academic Partnership. W.M., M.A.G. and J.W. acknowledge support from the ICE-ARC programme, European Union 7th Framework Programme, grant 603887. B.H. and J.W. acknowledge the ONR MIZ program (grants N000141410587 and N000141512338). M.A.G. was supported by the Centre for Ice, Climate and Ecosystems at the Norwegian Polar Institute and Norwegian Research Council project STASIS (grant 221961/F20). Finally this work could not have been performed without the help and support of the crew and officers of RV *Araon*. Observational data are available on the ICE-ARC data repository http://frazil.nerc-bas.ac.uk/ice-arc/csv.php?name=processed (IMB011 and IMB012), and simulation code and data from https://zenodo.org/record/1293459.

References

Burns, K. J., Vasil, G. M., Oishi, J. S., Lecoanet, D., & Brown, B. P. (2016). Dedalus: Flexible framework for spectrally solving differential equations, *Astrophysics Source Code Library*, record ascl:1603.015, http://ascl.net/1603.015, http://dedalus-project.org.

Carslaw, H. S., & Jaeger, J. C. (1959). *Conduction of heat in solids* (2nd edition). Oxford, UK: Oxford University Press.

Curry, J. A., Schramm, J. L., & Ebert, E. E. (1995). Sea ice-albedo climate feedback mechanism. *Journal of Climate*, *8*(2), 240–247.

Divine, D. V., Granskog, M. A., Hudson, S. R., Pedersen, C. A., Karlsen, T. I., Divina, et al. (2015). Regional melt-pond fraction and albedo of thin Arctic first-year drift ice in late summer. *The Cryosphere*, *9*(1), 255–268. http://doi.org/10.5194/tc-9-255-2015

Ebert, E. E., & Curry, J. A. (1993). An intermediate one-dimensional thermodynamic sea ice model for investigating ice-atmosphere interactions. *Journal of Geophysical Research: Oceans*, *98*(C6), 10085–10109. http://doi.org/10.1029/93JC00656

Fetterer, F., & Untersteiner, N. (1998). Observations of melt ponds on Arctic sea ice. *Journal of Geophysical Research: Oceans*, *103*(C11), 24821–24835. http://doi.org/10.1029/98JC02034

Flocco, D., & Feltham, D. L. (2007). A continuum model of melt pond evolution on Arctic sea ice. *Journal of Geophysical Research: Oceans*, *112*, C08016. http://doi.org/10.1029/2006JC003836

Frey, K. E., Perovich, D. K., & Light, B. (2011). The spatial distribution of solar radiation under a melting Arctic sea ice cover. *Geophysical Research Letters*, *38*(22), L22501. http://doi.org/10.1029/2011GL049421

Goluskin, D., & van der Poel, E. P. (2016). Penetrative internally heated convection in two and three dimensions. *Journal of Fluid Mechanics*, *791*, R6. http://doi.org/10.1017/jfm.2016.69

Hanesiak, J. M., Barber, D. G., De Abreu, R. A., & Yackel, J. J. (2001). Local and regional albedo observations of Arctic first-year sea ice during melt ponding. *Journal of Geophysical Research: Oceans*, *106*(C1), 1005–1016. http://doi.org/10.1029/1999JC000068

Hitchen, J. R., & Wells, A. J. (2016). The impact of imperfect heat transfer on the convective instability of a thermal boundary layer in a porous media. *Journal of Fluid Mechanics*, *794*, 154–174. http://doi.org/10.1017/jfm.2016.149

Hudson, S. R., Granskog, M. A., Sundfjord, A., Randelhoff, A., Renner, A. H. H., & Divine, D. V. (2013). Energy budget of first-year Arctic sea ice in advanced stages of melt. *Geophysical Research Letters*, *40*(11), 2679–2683. http://doi.org/10.1002/grl.50517

Hunke, E., Lipscomb, W., Turner, A., Jeffrey, N., & Elliot, S. (2015). *CICE: The Los Alamos sea ice model documentation and software user's manual version 5.1* (Report LA-CC-06-012). Los Alamos, NM: Los Alamos National Laboratory.

Jackson, K., Wilkinson, J., Maksym, T., Meldrum, D., Beckers, J., Haas, C., & Mackenzie, D. (2013). A novel and low-cost sea ice mass balance buoy. *Journal of Atmospheric and Oceanic Technology*, *30*(11), 2676–2688.

Kwok, R., & Untersteiner, N. (2011). The thinning of Arctic sea ice. *Physics Today*, *64*, 36. http://doi.org/10.1063/1.3580491

Lee, S. H., McRoy, C. P., Joo, H. M., Gradinger, R., Cui, X., Yun, M. S., et al. (2011). Holes in progressively thinning Arctic sea ice lead to new ice algae habitat. *Oceanography*, *24*(3), 302–308. http://doi.org/10.5670/oceanog.2011.81

Maykut, G. A. (1978). Energy exchange over young sea ice in the central Arctic. *Journal of Geophysical Research: Oceans*, *83*(C7), 3646–3658. http://doi.org/10.1029/JC083iC07p03646

McDougall, T. J., & Barker, P. M. (2011). Getting started with TEOS-10 and the Gibbs Seawater (GSW) Oceanographic Toolbox, 28pp., SCOR/IAPSO WG127, ISBN 978-0-646-55621-5.

Moon, W., & Wettlaufer, J. S. (2011). A low-order theory of Arctic sea ice stability. *Europhysics Letters*, *96*(3), 39001. http://doi.org/10.1209/0295-5075/96/39001

Nicolaus, M., Katlein, C., Maslanik, J., & Hendricks, S. (2012). Changes in Arctic sea ice result in increasing light transmittance and absorption. *Geophysical Research Letters*, *39*(24), L24501. http://doi.org/10.1029/2012GL053738

Pedersen, C. A., Roeckner, E., Lüthje, M., & Winther, J.-G. (2009). A new sea ice albedo scheme including melt ponds for ECHAM5 general circulation model. *Journal of Geophysical Research: Atmospheres, 114*, D08101. http://doi.org/10.1029/2008JD010440

Perovich, D. K., Grenfell, T. C., Light, B., Elder, B. C., Harbeck, J., Polashenski, C., et al. (2009). Transpolar observations of the morphological properties of Arctic sea ice. *Journal of Geophysical Research: Oceans, 114*, C00A04. http://doi.org/10.1029/2008JC004892

Perovich, D. K., Grenfell, T. C., Light, B., & Hobbs, P. V. (2002a). Seasonal evolution of the albedo of multiyear Arctic sea ice. *Journal of Geophysical Research: Oceans, 107*(C10), 8044. http://doi.org/10.1029/2000JC000438

Perovich, D. K., Nghiem, S. V., Markus, T., & Schweiger, A. (2007). Seasonal evolution and interannual variability of the local solar energy absorbed by the Arctic sea ice–ocean system. *Journal of Geophysical Research: Oceans*, *112*, C03005, http://doi.org/10.1029/2006JC003558

Perovich, D. K., & Polashenski, C. (2012). Albedo evolution of seasonal Arctic sea ice. *Geophysical Research Letters, 39*(8), L08501. http://doi.org/10.1029/2012GL051432

Perovich, D. K., Tucker III, W. B., & Ligett, K. A. (2002b). Aerial observations of the evolution of ice surface conditions during summer. *Journal of Geophysical Research: Oceans*, *107*(C10), 8048. http://doi.org/10.1029/2000JC000449

Polashenski, C., Perovich, D., & Courville, Z. (2012). The mechanisms of sea ice melt pond formation and evolution. *Journal of Geophysical Research: Oceans, 117*, C01001. http://doi.org/10.1029/2011JC007231

Skyllingstad, E. D., & Paulson, C. A. (2007). A numerical study of melt ponds. *Journal of Geophysical Research: Oceans, 112*, C08015. http://doi.org/10.1029/2006JC003729

Stramler, K. (2006). The influence of synoptic Arctic motions on the Arctic energy budget. *PhD thesis*, Columbia University, USA, 269pp.

Stroeve, J. C., Markus, T., Boisvert, L., Miller, J., & Barrett, A. (2014). Changes in Arctic melt season and implications for sea ice loss. *Geophysical Research Letters, 41*(4), 1216–1225. http://doi.org/10.1002/2013GL058951

Taylor, P. D., & Feltham, D. L. (2004). A model of melt pond evolution on sea ice. *Journal of Geophysical Research: Oceans, 109*, C12007. http://doi.org/10.1029/2004JC002361

Figure captions

Figure 1. (a) Map of the IMB drifting track with mean AMSR2 sea-ice concentration (%) during August 13–29, 2015, (b) aerial photo of the ice camp with the locations of ponds, (c) photos of two IMBs on August 13, and (d) schematic of instrument deployment with sensors including a vertical thermistor chain through air, pond, ice and upper ocean, along with shortwave radiometers (SW Rad.).

Figure 2. (a) Air temperature and (b) incoming shortwave radiation measured at the saline pond (blue) and the freshwater pond (red). The three periods P1–P3 are indicated by dashed vertical lines, with blue bars in (a) indicating snowfall events determined from the photographs. (c) Hourly evolution of vertical temperature profiles measured in the saline pond and (d–f) individual profiles at 02 UTC (close to the time of maximum water temperature) for three periods. (g–j) Same as (c–f) except for the freshwater pond. Note the isoline of freezing temperature of the saline pond of 20 g kg^{-1} salinity at −1.1 °C in (d–f), and the different scale in (h). In (c) and (g), the initiation of continuous surface freezing and snow accumulation is estimated based on the photographs.

Figure 3. Modeled heat transfer in freshwater and saline ponds for a nominal pond depth H = 0.1 m. (a) Scaled shape of heating profile predicted from the two-stream radiation model of SP07. A nonlinear equation of state predicts the variation of density with temperature for (b) a freshwater pond, and (c) a pond of uniform salinity 20 g kg^{-1}. Snapshots of simulated temperature for a convective flow with a nominal heating rate $Q_0H = 20$ W m^{-2} and $f = 0.5$ are illustrated for ponds with (d) freshwater, and (f) uniform salinity. Panel (e) shows that the horizontally and temporally averaged temperature profile $T(z)$ increases with shortwave flux in the pond interior, consistent with a diurnal cycle**,** where the internal heating rate Q_0H corresponds to 42% of the incident shortwave flux for the assumed heating model. Panel (g) compares the averaged $T(z)$ predicted for convective heat transfer when the pond has uniform salinity 20 g kg^{-1} (solid curve) and conductive heat transfer for a pond with a stable salt stratification (dashed curves) across a range of surface cooling factors $f = F_0/Q_0H$, with $Q_0H = 20$ W m^{-2}.

Figure 1.

(a)

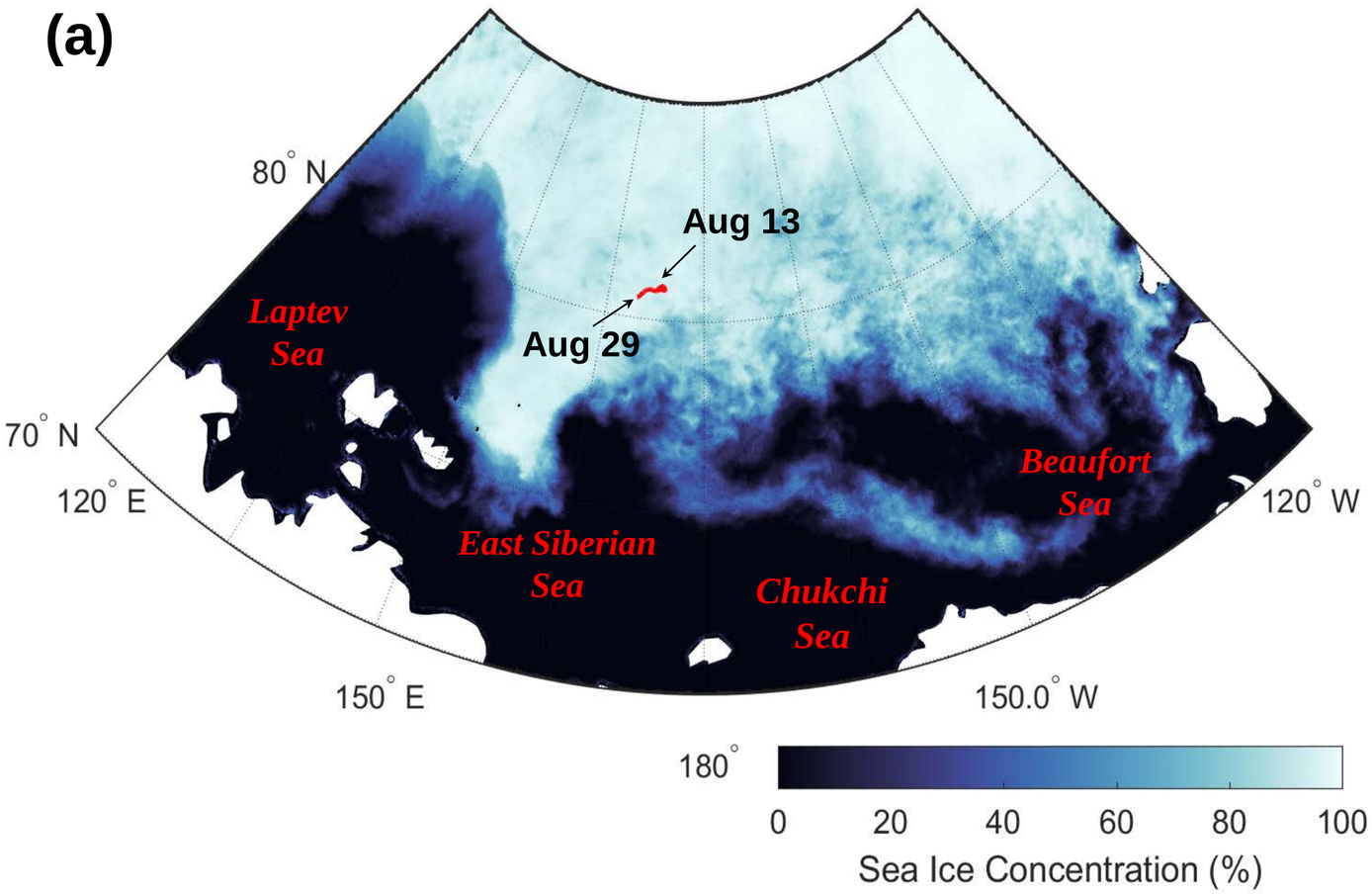
80° N
70° N
120° E
120° W
150° E
150.0° W
180°
Aug 13
Aug 29
Laptev Sea
East Siberian Sea
Chukchi Sea
Beaufort Sea
0
20
40
60
80
100
Sea Ice Concentration (%)

(b)

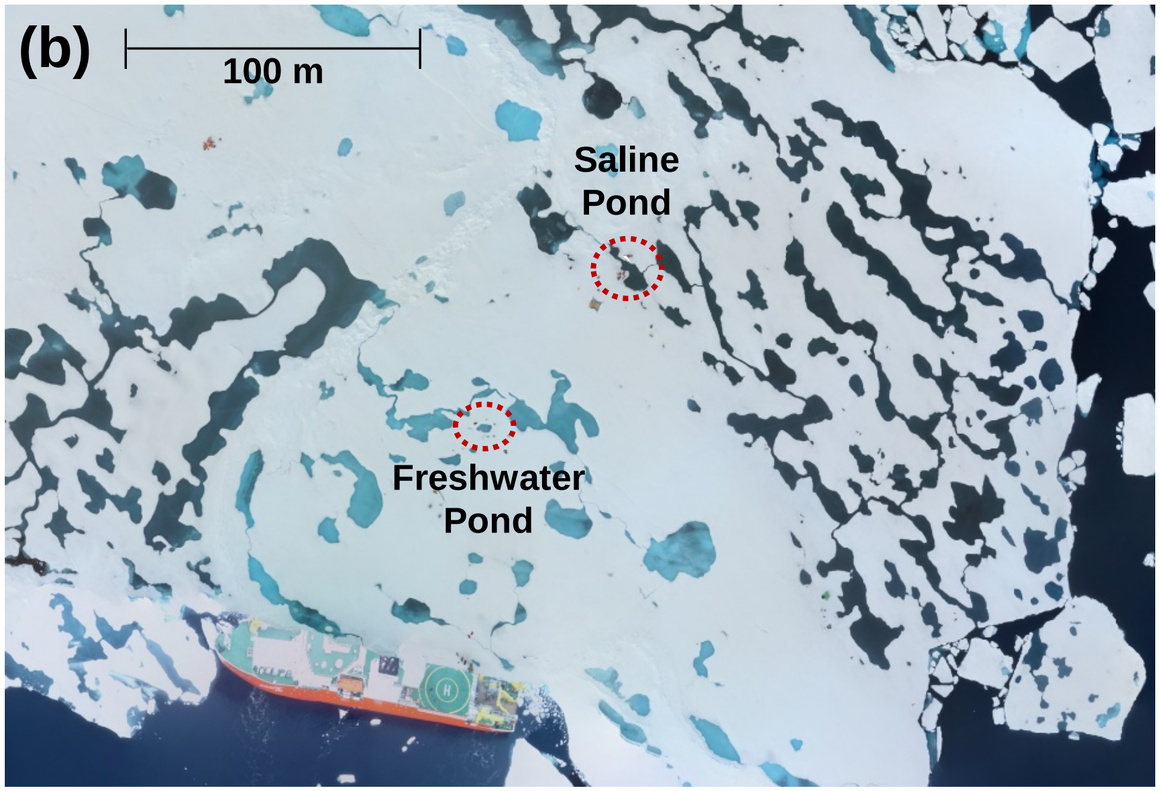
100 m
Saline Pond
Freshwater Pond

(c)

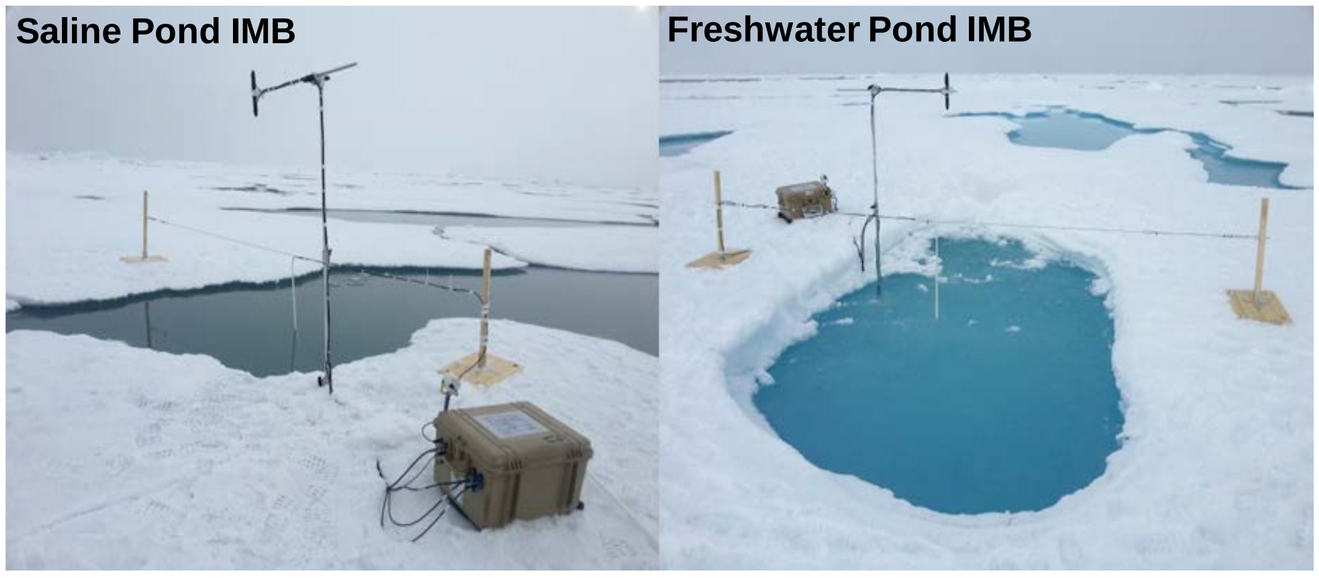
Saline Pond IMB
Freshwater Pond IMB

(d)

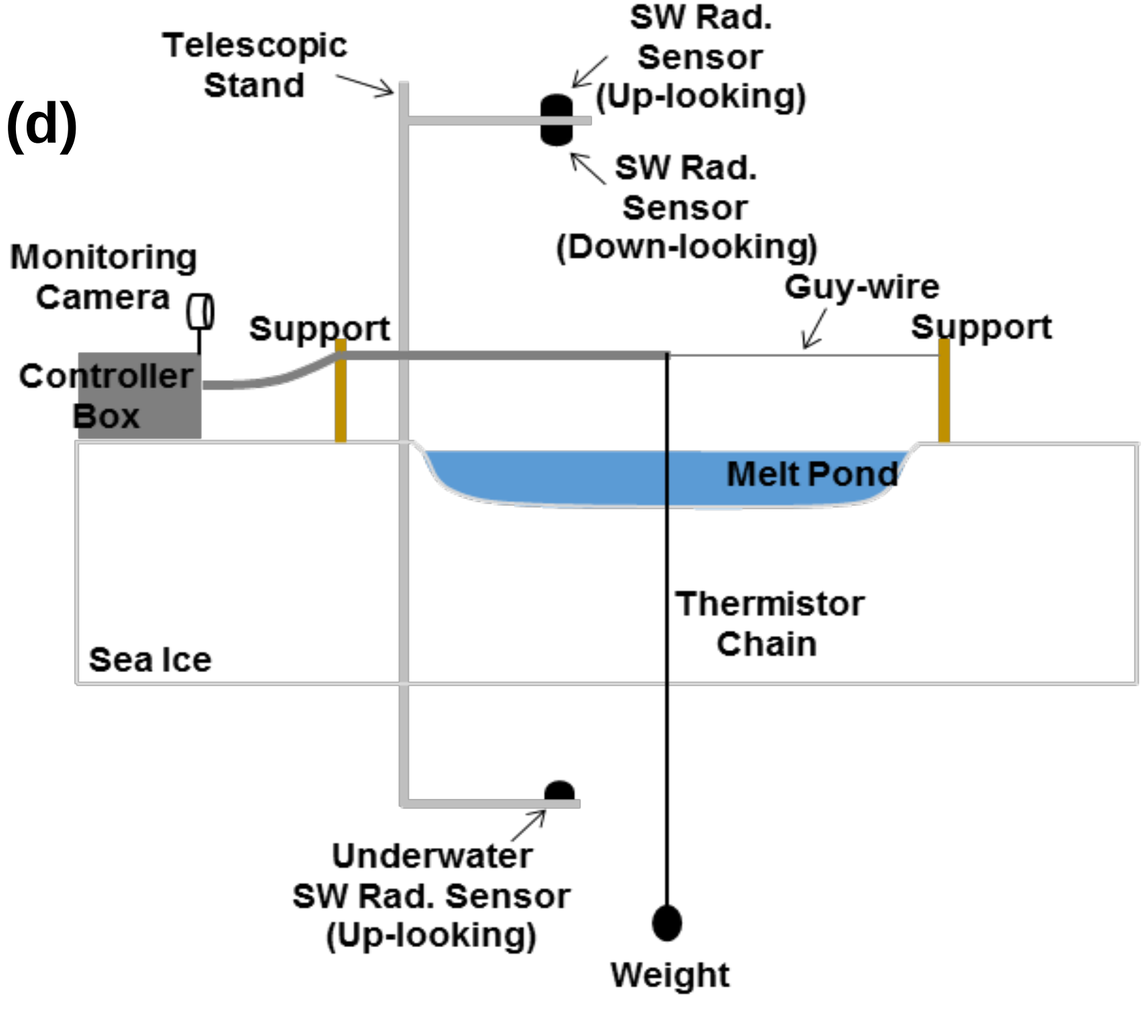
Telescopic Stand
SW Rad. Sensor (Up-looking)
SW Rad. Sensor (Down-looking)
Monitoring Camera
Support
Guy-wire
Support
Controller Box
Melt Pond
Thermistor Chain
Sea Ice
Underwater SW Rad. Sensor (Up-looking)
Weight

Figure 2.

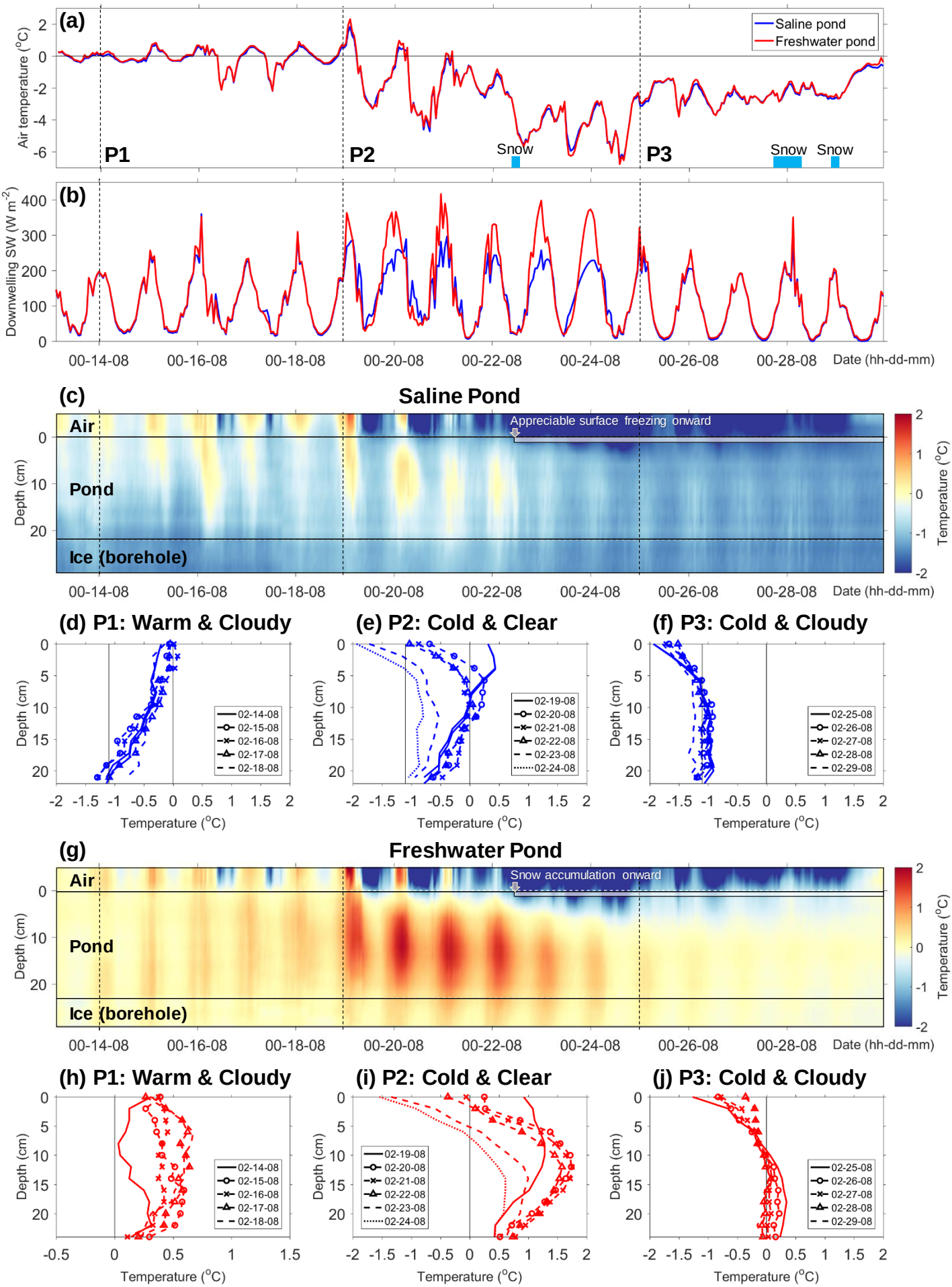
(a)
Air temperature (°C)
Saline pond
Freshwater pond
P1
P2
P3
Snow
Snow
Snow
(b)
Downwelling SW (W m-2)
00-14-08
00-16-08
00-18-08
00-20-08
00-22-08
00-24-08
00-26-08
00-28-08
Date (hh-dd-mm)
(c)
Saline Pond
Air
Pond
Ice (borehole)
Appreciable surface freezing onward
Depth (cm)
Temperature (°C)
(d) P1: Warm & Cloudy
(e) P2: Cold & Clear
(f) P3: Cold & Cloudy
02-14-08
02-15-08
02-16-08
02-17-08
02-18-08
02-19-08
02-20-08
02-21-08
02-22-08
02-23-08
02-24-08
02-25-08
02-26-08
02-27-08
02-28-08
02-29-08
Temperature (°C)
(g)
Freshwater Pond
Snow accumulation onward
(h) P1: Warm & Cloudy
(i) P2: Cold & Clear
(j) P3: Cold & Cloudy

Figure 3.

(a) Heating Profile

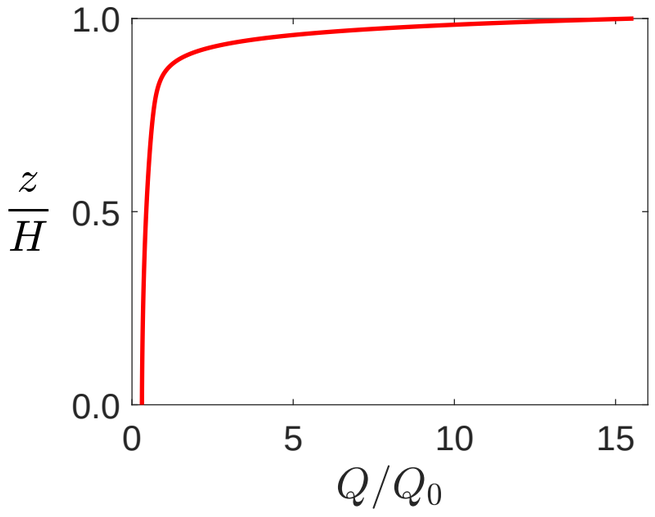

(b) Freshwater Density

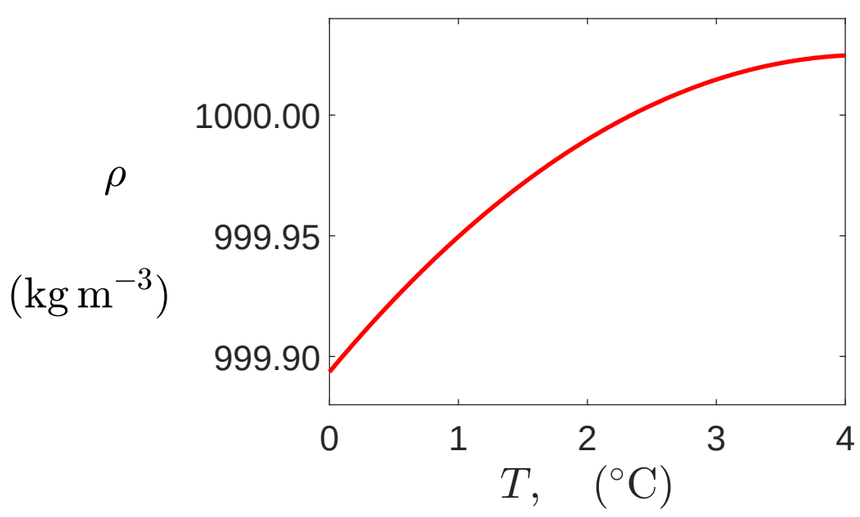

(c) 20 g kg^{-1} Saltwater Density

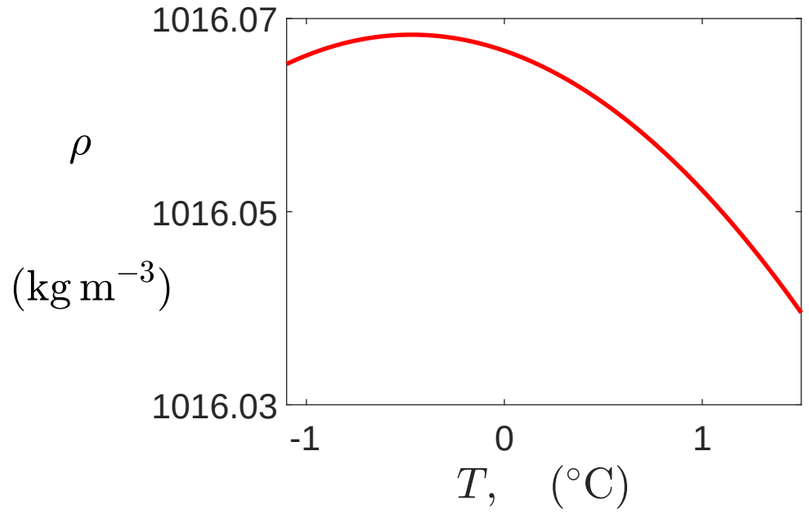

(d) Freshwater Pond

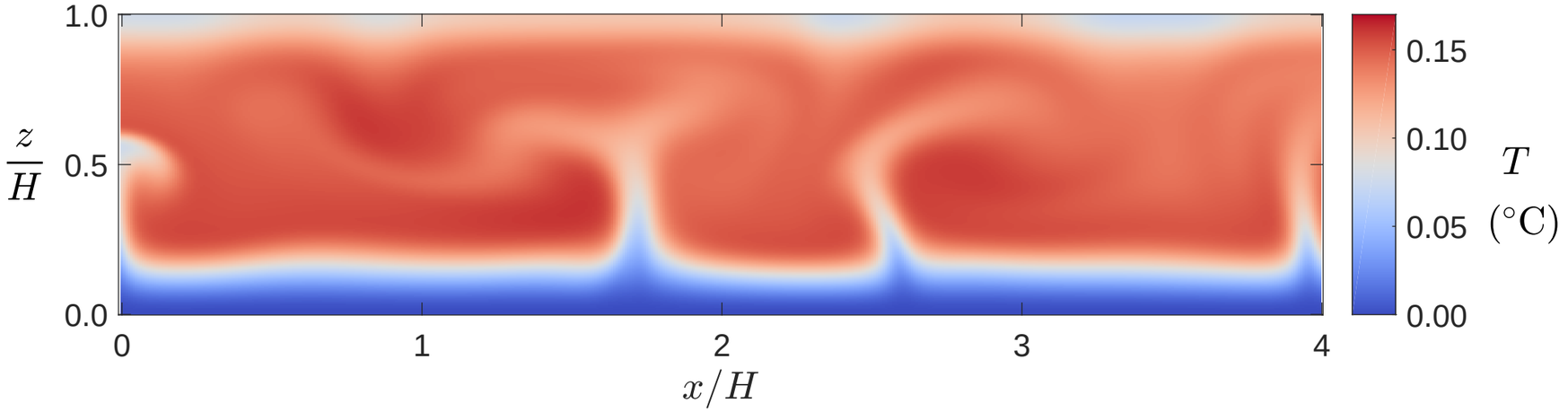

(e)

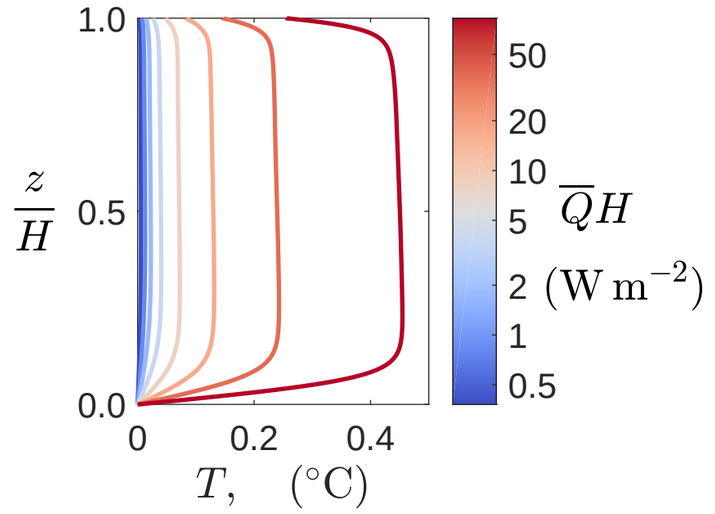

(f) 20 g kg^{-1} Saltwater Pond

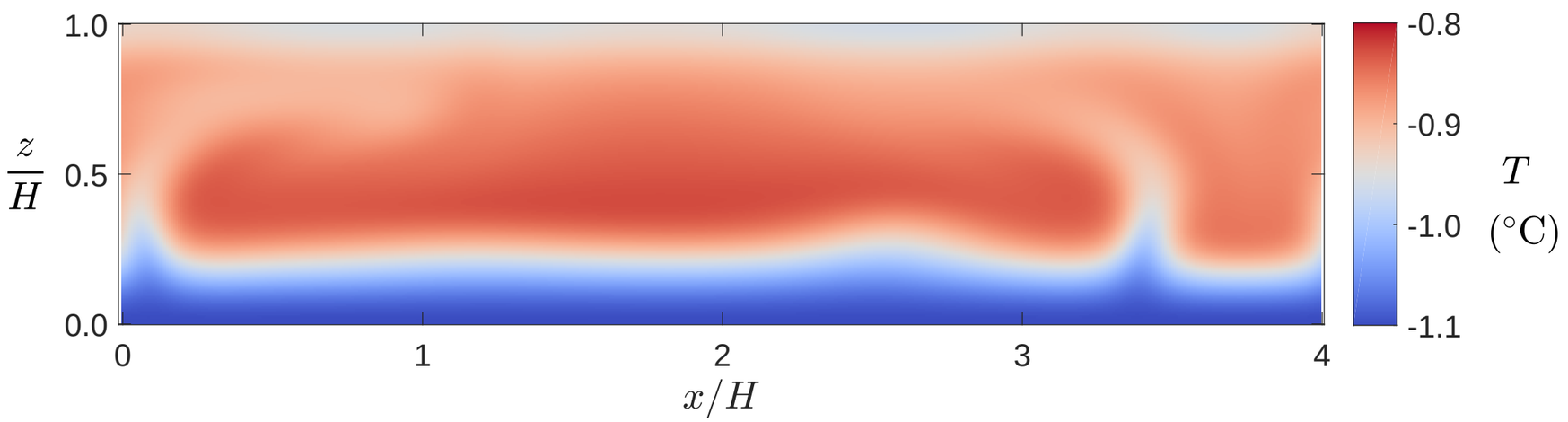

(g)